

REGULAR PAPER • OPEN ACCESS

Parametric optimization of depletion-type Si micro- ring modulator performances

Recent citations

- [Large-signal SPICE model for depletion-type silicon ring modulators](#)
Minkyu Kim *et al*

To cite this article: Younghyun Kim *et al* 2019 *Jpn. J. Appl. Phys.* **58** 062006

View the [article online](#) for updates and enhancements.



Parametric optimization of depletion-type Si micro-ring modulator performances

Younghyun Kim¹, Youngkwan Jo¹, Minkyu Kim¹, Byung-Min Yu¹, Christian Mai², Stefan Lischke², Lars Zimmermann², and Woo-Young Choi^{1*}

¹Department of Electrical and Electronic Engineering, Yonsei University, Seoul 120-749, Republic of Korea

²Innovations for High Performance Microelectronics, 15236 Frankfurt (Oder), Germany

*E-mail: wchoi@yonsei.ac.kr

Received February 19, 2019; revised May 14, 2019; accepted May 19, 2019; published online June 6, 2019

We present the modulation performance optimization process for a depletion-type Si micro-ring modulator (MRM). Our optimization process is based on two different types of model parameters for ring resonator decay time constants derived from the coupled-mode theory. The MRM figure of merit (FOM) is defined for target data rates considering both optical modulation amplitude and the modulation frequency response based on two model parameters. The parametric optimization for modulator output eye diagrams is achieved by analyzing the FOM with MRM simulation with varying two model parameters. In addition, we demonstrate the optimized eye diagram can be achieved with our optimization process and the measurement results agree well with the simulation result. © 2019 The Japan Society of Applied Physics

1. Introduction

Si Photonics has attracted great attention due to the large-scale photonic integration capability, which enables future computing systems with low-power and high-speed optical interconnects.^{1,2)} Among several key building blocks used for Si photonic interconnect systems, Si optical modulators play an important role for high data rates. The carrier-induced refractive-index change is commonly used for the Si modulators by means of carrier injection, depletion and accumulation, and then a light intensity or phase is modulated through a Mach-Zehnder interferometer and a micro-ring resonator.³⁾

Depletion-type Si micro-ring modulators (MRM) are actively investigated as an important device for high-performance optical interconnect systems based on Si Photonics because they can provide large modulation bandwidths and small device footprints, which are highly attractive for cost-effective co-integration of photonics and electronics.⁴⁾ The performances of Si MRM have been improved and experimentally demonstrated in perspectives of high-speed modulation,^{5,6)} high energy efficiency,^{7,8)} increased transmission capacity using advanced modulation formats⁹⁻¹¹⁾ and bandwidth enhancement using optical peaking¹²⁾ or cascaded micro-ring structures.^{13,14)} In addition, there have been several reports for analyses¹⁵⁻²⁰⁾ and modeling of Si MRMs.²¹⁻²⁷⁾ In particular, the tradeoff between Si MRM modulation bandwidth and optical modulation amplitude (OMA) was investigated based on the small-signal model which is obtained from the coupled-mode equation in.²⁰⁾ However, there has not been any report that provides the systematic device design guideline for the optimal eye performance given the target data rate. In this paper, we present such an optimization technique based on simple Si MRM device parameters.

This paper is organized as follows. In Sect. 2, we briefly introduce the Si MRM model based on the coupled-mode theory from which an analytical expression for the modulation frequency response containing key model parameters is obtained. In Sect. 3, we explain the Si MRM performance

optimization process based on the model parameters. In Sect. 4, we show the experimental verification. Section 5 concludes the paper.

2. Si MRM model

With the coupled-mode theory, the dynamics of a Si MRM can be described as²⁸⁾

$$\frac{d}{dt}a(t) = \left(j\omega_{\text{res}} - \frac{1}{\tau} \right) a(t) - j\sqrt{\frac{2}{\tau_c}} E_{\text{in}}(t), \quad (1)$$

$$E_{\text{out}}(t) = E_{\text{in}}(t) - j\sqrt{\frac{2}{\tau_c}} a(t), \quad (2)$$

where a is the amplitude of the energy stored in the ring resonator, ω_{res} is the resonance angular frequency, τ is the decay time constant for the stored energy. τ is given as $1/(1/\tau_1 + 1/\tau_c)$ where τ_1 represents the decay time constant due to the loss in the ring resonator, and τ_c due to coupling with the directional coupler. E_{in} is the input and E_{out} is the output optical field.

The steady-state characteristics can be derived from (1) as²¹⁾

$$\left(\frac{E_{\text{out}}}{E_{\text{in}}} \right)^2 = \left(\frac{j(\omega - \omega_{\text{res}}) + \frac{2}{\tau_1} - \frac{1}{\tau}}{j(\omega - \omega_{\text{res}}) + \frac{1}{\tau}} \right)^2. \quad (3)$$

With the small-signal approximation of Eqs. (1) and (2), $\Delta_o(s)$, the modulation frequency response of a Si MRM in the s -domain can be given as^{22,29)}

$$\Delta_o(s) = \frac{4}{n_0} \cdot \frac{\partial n_{\text{eff}}}{\partial V_j} \cdot \frac{\omega_{\text{res}} D / \tau_c}{D^2 + 1/\tau^2} \cdot \frac{s + 2/\tau_1}{s^2 + (2/\tau)s + D^2 + 1/\tau^2}. \quad (4)$$

Here, V_j is the voltage applied across the p-n junction in the Si MRM, D defined as $|\omega_{\text{res}} - \omega_{\text{in}}|$ represents how much the input light angular frequency, ω_{in} , is detuned from ω_{res} . n_0 and n_{eff} are the unperturbed and effective refractive-index,



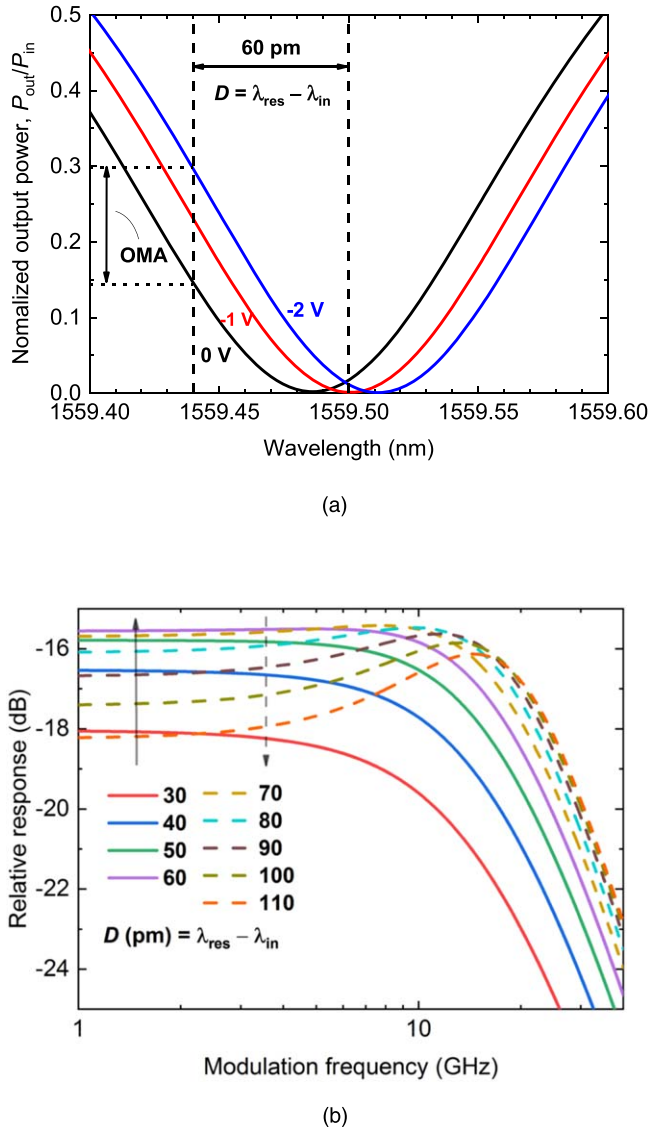


Fig. 1. (Color online) (a) Steady-state transmission characteristics with variable reverse bias voltages, and (b) E/O frequency responses with different detuning wavelengths for fabricated Si MRM.

respectively. It is important to notice that the MRM modulation frequency response is determined by a few key parameters, with which modulator performance optimization can be achieved.

3. Performance optimization

Figure 1(a) shows the simulated Si MRM steady-state transmission characteristics and Fig. 1(b) the modulation frequency responses for a sample Si MRM. For bias voltages of 0, -1, -2 V, the values of modeling parameters (τ_1 , τ_e) are obtained as 22.42 ps rad⁻¹, 22.88 ps rad⁻¹, 23.12 ps rad⁻¹ for τ_1 , and 24.65 ps rad⁻¹, 24.62 ps rad⁻¹, 24.65 ps rad⁻¹ for τ_e , respectively. Also, the values of n_{eff} are 2.637 124, 2.637 150 and 2.637 167 for each bias voltage.²³⁾ The device has the lateral p-n junction diode waveguide structure as in²³⁾ with the nominal peak doping concentration of 7×10^{17} cm⁻³ for p-region and 3×10^{18} cm⁻³ for n-region.

It is important to consider the detuning parameter, D because device performance is highly dependent on it. For

the operating wavelength, D is 60 pm with the decay time constants to maximize OMA. It is known that the steady-state OMA is maximized when $D = (3^{1/2}\tau)^{-1}$,³⁰⁾ which can be also deduced by introducing $s = 0$ in (4).

Also, the modulation bandwidth becomes maximally flat at $D = 60$ pm as can be seen Fig. 1(b). In detail, DC gain which refers to small-signal gain in the low modulation frequency and bandwidth increase with increasing D and they are maximized at 60 pm. After 60 pm, the bandwidth still increases but with sacrificing DC gain. Therefore, we used the D to maximize DC gain as well as the bandwidth. Here, the modulation bandwidth was calculated with consideration to Si MRM electrical properties. The transfer function for electrical parts is given as

$$\Delta_E(s) = \frac{1/sC_{cc}}{sL_{\text{int}} + R_{\text{int}} + 1/sC_{cc}} \cdot \frac{1/sC_j}{R_s + 1/sC_j},$$

where C_{cc} is the capacitance between n⁺ to p⁺ metal contact, C_j the p-n junction capacitance, R_s the series resistance, L_{int} and R_{int} the inductance and resistance due to interconnection from pads to metal contacts.

Details of electrical properties of the Si MRM can be found in^{23,24)} and calculated electrical 3 dB bandwidth using (5) with measured values for circuit parameters is about 62 GHz. With this electrical 3 dB bandwidth, its influence on the Si MRM dynamics for 25 and 50 Gbps operations is not significant. Although each of C_j and R_s is influenced by the ring size, their product is not because C_j is proportional to the ring circumference but R_s is inversely proportional to the ring circumference. Consequently, the results of our analysis should be valid for Si MRMs with different sizes as long as the doping concentrations are the same.

In the same way, the normalized OMA which refers to OMA normalized by the input optical power ($P_{\text{out}}/P_{\text{in}}$) and the bandwidth can be calculated by many different kinds of resonance conditions with various τ_1 and τ_e . We show the simulated results for normalized OMA and 3 dB bandwidth as a function of τ_1 and τ_e in Figs. 2(a) and 2(b), respectively. As τ_1 and τ_e increase, the OMA increases until it reaches its optimum value, as can be seen in Fig. 2(a) but the bandwidth decreases in Fig. 2(b), showing the tradeoff between OMA and bandwidth relates to the Q factor of the ring resonator.

The saturated OMA along with τ_e is due to the small resonance despite the high Q factor.

In order to obtain the optimized eye diagram, we introduce a figure of merit (FOM) defined as below

$$\text{FOM} = \text{Normalized OMA} \times f(BW), \quad (5)$$

$$f(BW) = \begin{cases} BW & (BW < DR \times 0.7) \\ DR \times 0.7 & (BW \geq DR \times 0.7) \end{cases}, \quad (6)$$

where BW is the 3 dB bandwidth divided by GHz, and DR is the target data rate divided by Gbps. The saturation function is used for $f(BW)$ since the modulator bandwidth does not have to be larger than about 70% of the data rate for NRZ modulation format.³¹⁾

Figure 3 shows the calculated FOM with varying τ_1 and τ_e values for three different data rates of 12.5, 25, and 50 Gbps. The FOM dependence on τ_1 and τ_e for 12.5 Gbps as shown in

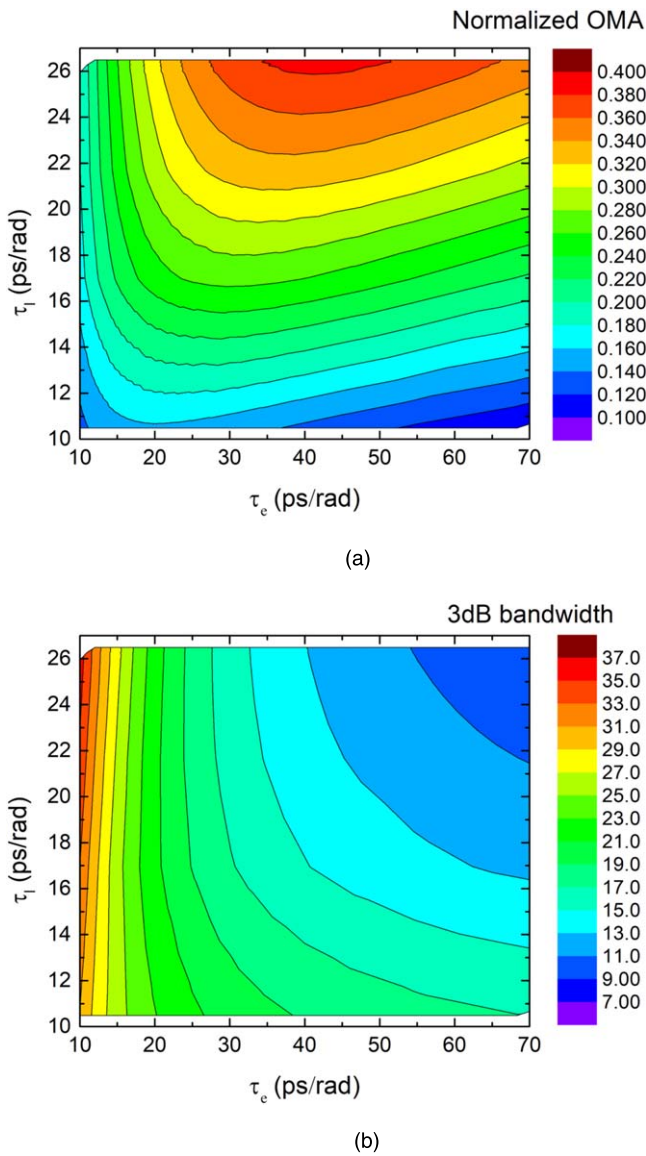


Fig. 2. (Color online) (a) Normalized OMA and (b) 3 dB bandwidth in GHz as a function of τ_1 and τ_e .

Fig. 3(a) is similar to the normalized OMA as shown in Fig. 2(a) since the bandwidth does not have much influence due to the low data rate. However, for larger data rates of 25 and 50 Gbps, the optimal τ_e value moves to the lower value since more bandwidth is required than the OMA.

To investigate the relationship between the FOM and the eye diagrams under various conditions, we also simulated eye diagrams by numerically solving (1) and (2). The details can be found in,²⁴⁾ where the accuracy of our ring modulator model was confirmed. Figure 4 shows the simulated 25 Gbps eye diagrams at different τ_1 and τ_e values for six different points shown in Fig. 3(b). Among them, point B having the largest FOM produces the largest eye opening. The bandwidth is large enough for point A but the limited eye opening occurs because the OMA is too low. For point b, c, and d, the bandwidth is sufficient but the eye opening is smaller due to smaller OMA with the decreasing τ_1 value. Simulated 50 Gbps eye diagrams with different τ_1 and τ_e values are shown in Fig. 5. Compared to 25 Gbps data operation, a

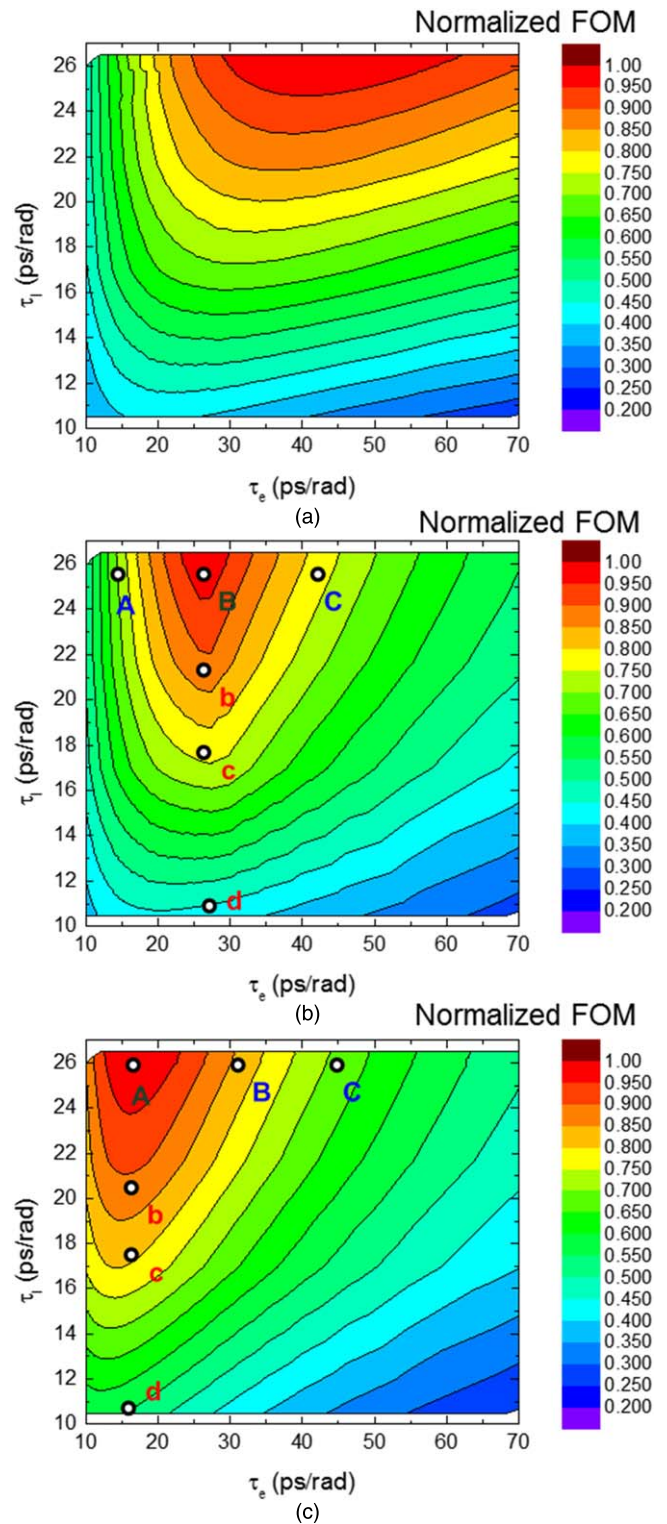


Fig. 3. (Color online) Normalized FOM as a function of τ_1 and τ_e for certain target data rates of (a) 12.5, (b) 25, and (c) 50 Gbps.

larger bandwidth is required and, consequently, a larger value for τ_e , results in the clearest eye diagram, for point A in Fig. 5(c). As shown in Figs. 5(b) and 5(c), the eye opening becomes smaller even with the larger OMA due to the lack of bandwidth at point B and C, respectively. For points b, c, and d in Fig. 3(c) with corresponding eye diagrams in Figs. 5(d)–5(f), eye diagrams are clean with sufficient bandwidth but the opening is small due to smaller OMA.

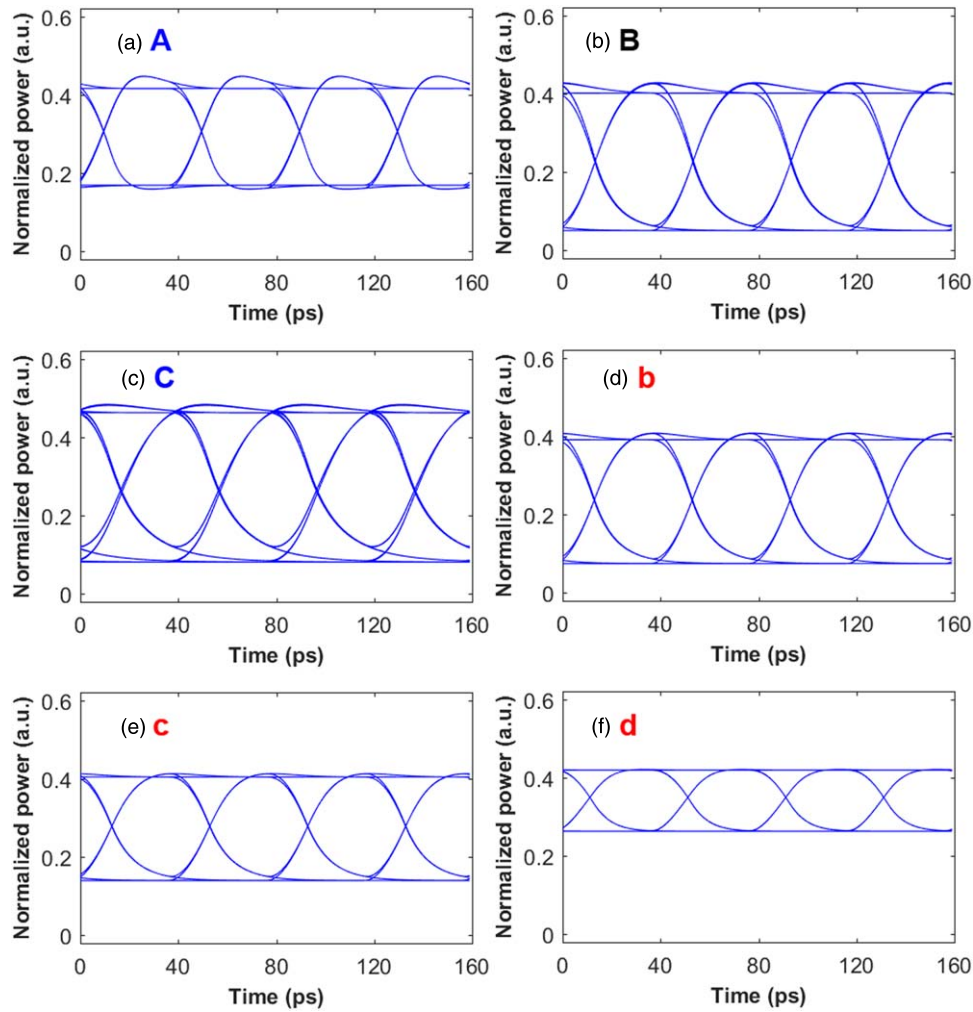


Fig. 4. (Color online) Simulated eye diagrams for 25 Gbps PRBS $2^7 - 1$ patterns with different τ_1 and τ_c values at (a) A, (b) B, (c) C, (d) b, (e) c, and (f) d of Fig. 3(b).

4. Experimental verification

The device fabricated by Innovations for high-performance microelectronics is used for experimental verification.³²⁾ Figures 6(a) and 6(b) show the optical microscopy images of the fabricated Si MRM. In order to verify our optimization process, we designed a Si MRM for 25 Gbps operation which requires $\tau_1 = 26.40$ and $\tau_c = 25.36$ ps rad⁻¹ roughly corresponding to point B in Fig. 3(b). The device has 8 μ m radius and the doped-Si waveguide has 32.23 dB cm⁻¹ of round-trip loss with the nominal peak doping concentration of 7×10^{17} cm⁻³ for p-region and 3×10^{18} cm⁻³ for n-region. In addition, the field-ratio of the coupled light at the directional coupler is 0.1889, with which Q factor of several thousand can be achieved for the ring resonator. Figures 7(a) and 7(b) show the simulated and measured eye diagrams with 25 Gbps PRBS $2^7 - 1$ patterns without any pre-emphasis, $2 V_{\text{peak-to-peak}}, -1 V_{\text{DC}}, 60$ pm for D , respectively. For the simulated eye diagram, we included the effect of equipment's bandwidth (about 18 GHz) by adding one-pole low-pass filter. The input optical power was kept less than 0.025 mW in order to avoid any asymmetric dynamic OMA of the Si MRM due to self-heating²¹⁾.

The input data provided by the pattern generator (Anritsu MP1800A) drives the Si MRM device without any termination. Since the Si MRM is very small, it can be taken as a lumped element (a capacitive load) and can be driven without any termination resistor. As it can be seen, they show good agreement, having 4.48 dB extinction ratio, which satisfies specifications required for 100 G PSM4³³⁾ and CWDM³⁴⁾ applications, indicating the effectiveness of the parametric optimization for Si MRMs.

5. Conclusion

We demonstrate the parametric optimization process for the depletion-type Si MRM modulation performance. Using the data rate dependent FOM with modeling parameters, τ_1 and τ_c , it is possible to optimize the eye diagrams for a target data rate. We numerically determine the FOMs for 12.5, 25, and 50 Gbps data rates, in which the condition for the optimized FOM produces the best eye diagram. In addition, we confirm the accuracy of our optimization process by measuring a 25 Gbps Si MRM eye diagram. Our technique can be used as a very useful design guide for realizing high-performance Si MRMs.

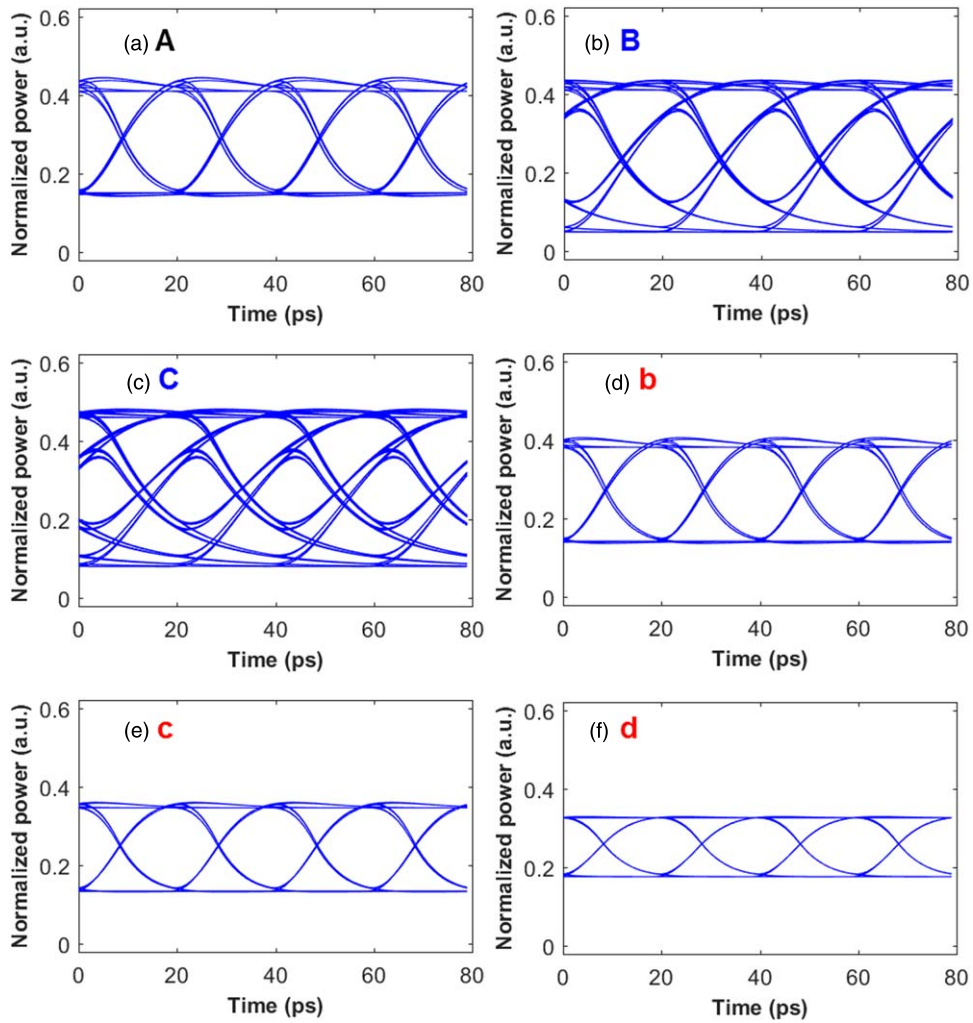


Fig. 5. (Color online) Simulated eye diagrams for 50 Gbps PRBS $2^7 - 1$ patterns with different τ_1 and τ_c values at (a) A, (b) B, (c) C, (d) b, (e) c, and (f) d of Fig. 3(c).

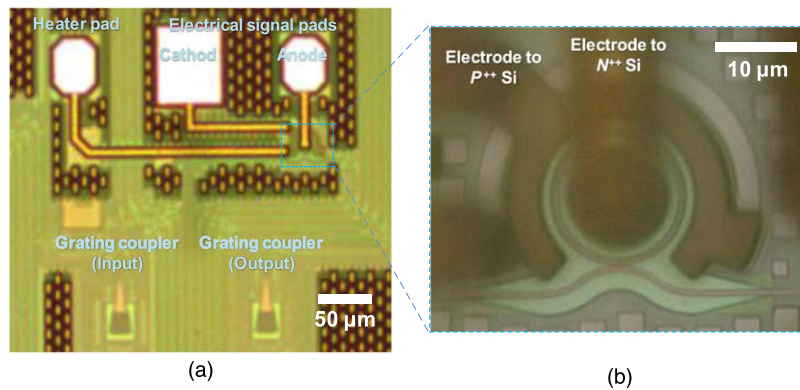


Fig. 6. (Color online) Optical microscopy image of (a) fabricated Si MRM with electrical signal pads and optical input/output and (b) enlarged Si MRM.

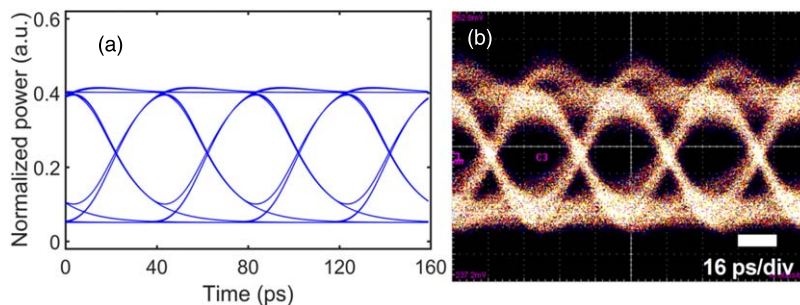


Fig. 7. (Color online) (a) Simulated and (b) measured eye diagrams for 25 Gbps PRBS $2^7 - 1$ patterns at $\tau_1 = 26.40 \text{ ps rad}^{-1}$ and $\tau_c = 25.36 \text{ ps rad}^{-1}$ in optimized FOM.

ORCID iDs

Younghyun Kim  <https://orcid.org/0000-0001-8072-1251>Youngkwon Jo  <https://orcid.org/0000-0002-6351-7213>

- 1) P. P. Absil, P. Verheyen, P. De Heyn, M. Pantouvaki, G. Lepage, J. D. Coster, and J. V. Campenhout, "Silicon photonics integrated circuits: a manufacturing platform for high density, low power optical I/O's," *Opt. Express* **23**, 9369 (2015).
- 2) M. Pantouvaki et al., "Active components for 50 Gb/s NRZ-OOK optical interconnects in a silicon photonics platform," *J. Lightwave Technol.* **35**, 631 (2016).
- 3) G. T. Reed, G. Mashanovich, F. Y. Gardes, and D. J. Thomson, "Silicon optical modulators," *Nat. Photonics* **4**, 518 (2010).
- 4) P. Dong et al., "Low V-pp, ultralow-energy, compact, high-speed silicon electro-optic modulator," *Opt. Express* **17**, 22484 (2009).
- 5) X. Xiao, X. Li, H. Xu, Y. Hu, K. Xiong, Z. Li, T. Chu, J. Yu, and Y. Yu, "44 Gb s⁻¹ silicon microring modulators based on zigzag PN junctions," *IEEE Photonics Technol. Lett.* **24**, 1712 (2012).
- 6) M. Pantouvaki, P. Verheyen, J. De Coster, G. Lepage, P. Absil, and J. V. Campenhout, "56 Gb s⁻¹ ring modulator on a 300 mm silicon photonics platform," Proc. IEEE Eur. Conf. Opt. Commun. (ECOC), 2015, p. 1.
- 7) J. C. Rosenberg et al., "Low-power 30 Gbps silicon microring modulator," CLEO: 2011—Laser Science to Photonic Applications, 2011 (Baltimore, MD), p. 1.
- 8) G. Li et al., "25 Gb s⁻¹ 1V-driving CMOS ring modulator with integrated thermal tuning," *Opt. Express* **19**, 20435 (2011).
- 9) S. Pitris et al., "A 4×40 Gb s⁻¹ O-band WDM silicon photonic transmitter based on micro-ring modulators," Optical Fiber Communication Conf. (OFC) 2019, OSA Technical Digest, 2019 (Optical Society of America) paper W3E.2.
- 10) H. Li et al., "A 112 Gb s⁻¹ PAM4 transmitter with silicon photonics microring modulator and CMOS driver," Optical Fiber Communication Conf. Postdeadline Papers 2019 (Optical Society of America) paper Th4A.4.
- 11) P. Dong et al., "Experimental demonstration of microring quadrature phase-shift keying modulators," *Opt. Lett.* **37**, 1178 (2012).
- 12) J. Muller et al., "Optical peaking enhancement in high-speed ring modulators," *Sci. Rep.* **4**, 6310 (2014).
- 13) Y. Li et al., "Coupled-ring-resonator-based silicon modulator for enhanced performance," *Opt. Express* **16**, 13342 (2008).
- 14) Y. Hu et al., "High-speed silicon modulator based on cascaded microring resonators," *Opt. Express* **20**, 15079 (2012).
- 15) W. D. Sacher and J. K. S. Poon, "Dynamics of microring resonator modulators," *Opt. Express* **16**, 15741 (2008).
- 16) W. D. Sacher et al., "Characteristics of microring resonators with waveguide-resonator coupling modulation," *J. Lightwave Technol.* **27**, 3800 (2009).
- 17) B. E. Little et al., "Microring resonator channel dropping filters," *J. Lightwave Technol.* **15**, 998 (1997).
- 18) W. Bogaerts et al., "Silicon microring resonators," *Laser Photonics Rev.* **6**, 47 (2012).
- 19) G. Li et al., "Ring resonator modulators in silicon for interchip photonic links," *IEEE J. Sel. Top. Quantum Electron.* **19**, 95 (2013).
- 20) H. Yu et al., "Trade-off between optical modulation amplitude and modulation bandwidth of silicon micro-ring modulators," *Opt. Express* **22**, 15178 (2014).
- 21) M. Shin et al., "Parametric characterization of self-heating in depletion-type Si micro-ring modulators," *IEEE J. Sel. Top. Quantum Electron.* **22**, 6 (2016).
- 22) B. Pile and G. Taylor, "Small-signal analysis of microring resonator modulators," *Opt. Express* **22**, 14913 (2014).
- 23) M. Shin et al., "A linear equivalent circuit model for depletion-type silicon microring modulators," *IEEE Trans. Electron Devices* **64**, 1140 (2017).
- 24) J. Rhim et al., "Verilog-A behavioral model for resonance-modulated silicon micro-ring modulator," *Opt. Express* **23**, 8762 (2015).
- 25) R. Dube-Demers et al., "Analytical modeling of silicon microring and microdisk modulators with electrical and optical dynamics," *J. Lightwave Technol.* **33**, 4240 (2015).
- 26) S. Lin et al., "Electronic-photonics co-optimization of high-speed silicon photonic transmitters," *J. Lightwave Technol.* **35**, 4766 (2017).
- 27) M. Kim et al., "A large-signal equivalent circuit for depletion-type silicon ring modulators," Proc. Opt. Fiber Commun. Conf. (OFC), 2018p. Th2A.13.
- 28) H. A. Haus, "Coupling of modes—resonators and couplers," *Waves and Fields in Optoelectronics* (Prentice-Hall, Englewood Cliffs, NJ, 1984), p. 07632.
- 29) Y. Ban et al., "Small-signal frequency responses for Si micro-ring modulators," Proc. IEEE Opt. Interconnects Conf., 2014, p. 47.
- 30) H. Yu et al., "Trade-off between optical modulation amplitude and modulation bandwidth of silicon micro-ring modulators," *Opt. Express* **22**, 15178 (2015).
- 31) Mindspeed Technologies, "NRZ bandwidth (-3 db HF cutoff vs SNR) how much bandwidth is enough?" White paper, Tech. Rep. 02XXX-WTP-001-A, 2003.
- 32) D. Knoll et al., "SiGe BiCMOS for optoelectronics (invited)," *ECS Trans.* **75**, 121 (2016).
- 33) 100G PSM4 Specification, PSM4-MSA.
- 34) 100G CWDM Spec, CWDM4-MSA.